

# A Laser-Driven Microrobot for Thermal Stimulation of Single Cells

Philipp Harder, Nergishan İyisan, Chen Wang, Fabian Kohler, Irina Neb, Harald Lahm, Martina Drefßen, Markus Krane, Hendrik Dietz, and Berna Özkale\*

Here, the study presents a thermally activated cell-signal imaging (TACSI) microrobot, capable of photothermal actuation, sensing, and light-driven locomotion. The plasmonic soft microrobot is specifically designed for thermal stimulation of mammalian cells to investigate cell behavior under heat active conditions. Due to the integrated thermosensitive fluorescence probe, Rhodamine B, the system allows dynamic measurement of induced temperature changes. TACSI microrobots show excellent biocompatibility over 72 h in vitro, and they are capable of thermally activating single cells to cell clusters. Locomotion in a 3D workspace is achieved by relying on thermophoretic convection, and the microrobot speed is controlled within a range of 5–65  $\mu\text{m s}^{-1}$ . In addition, light-driven actuation enables spatiotemporal control of the microrobot temperature up to a maximum of 60 °C. Using TACSI microrobots, this study targets single cells within a large population, and demonstrates thermal cell stimulation using calcium signaling as a biological output. Initial studies with human embryonic kidney 293 cells indicate a dose dependent change in intracellular calcium content within the photothermally controlled temperature range of 37–57 °C.

relies on biocompatible plasmonic agents to transduce light into heat, which eliminates diseased tissue in a highly localized manner.<sup>[1,2]</sup> Delivering large populations of photothermally active nanoagents to the diseased site can kill solid tumors and bacteria in infected diabetic ulcers, via noxious heat.<sup>[3–5]</sup> Moreover, regulating the heat dose to mild levels has been shown to significantly enhance wound healing.<sup>[6,7]</sup> Furthermore, neuromodulation via photothermal heating was recently proposed as a therapeutic strategy to prevent ventricular arrhythmias and to treat depression.<sup>[8,9]</sup> While these examples highlight the versatility of the technology, a comprehensive understanding of cell response to heat is lacking. Deciphering this relationship is necessary for the efficient use of photothermal stimulation in medicine.

A wide range of technologies have been developed to investigate thermal biology in general and to probe cell responses to local changes in temperature. Early work demonstrated the heat-sensitive dynamics of Transient Receptor Potential (TRP) channels, using heating elements to subject cell populations to global changes in temperature.<sup>[10,11]</sup> In combination with advanced

## 1. Introduction

Photothermal stimulation has enabled a new class of therapeutic strategies, applicable to a wide range of diseases. The strategy

P. Harder, N. İyisan, C. Wang, B. Özkale  
Microrobotic Bioengineering Lab (MRBL)  
School of Computation Information and Technology  
Technical University of Munich  
Hans-Piloty-Straße 1, 85748 Garching, Germany  
E-mail: berna.oezkale@tum.de

P. Harder, N. İyisan, C. Wang, B. Özkale  
Munich Institute of Robotics and Machine Intelligence  
Technical University of Munich  
Georg-Brauchle-Ring 60, 80992 Munich, Germany


P. Harder, N. İyisan, C. Wang, F. Kohler, H. Dietz, B. Özkale  
Munich Institute of Biomedical Engineering  
Technical University of Munich  
Boltzmannstraße 11, 85748 Garching, Germany

F. Kohler, H. Dietz  
Laboratory for Biomolecular Nanotechnology  
School of Natural Sciences  
Technical University of Munich  
Am Coulombwall 4a, 85748 Garching, Germany

I. Neb, H. Lahm, M. Drefßen  
Institute for Translational Cardiac Surgery (INSURE)  
Department of Cardiovascular Surgery  
German Heart Center  
Technical University of Munich  
80636 Munich, Germany

M. Krane  
Division of Cardiac Surgery  
Yale School of Medicine  
New Haven, CT 06510, USA

M. Krane  
DZHK (German Center for Cardiovascular Research)  
Partner site Munich Heart Alliance  
80802 Munich, Germany

 The ORCID identification number(s) for the author(s) of this article can be found under <https://doi.org/10.1002/adhm.202300904>

© 2023 The Authors. Advanced Healthcare Materials published by Wiley-VCH GmbH. This is an open access article under the terms of the Creative Commons Attribution-NonCommercial License, which permits use, distribution and reproduction in any medium, provided the original work is properly cited and is not used for commercial purposes.

DOI: 10.1002/adhm.202300904

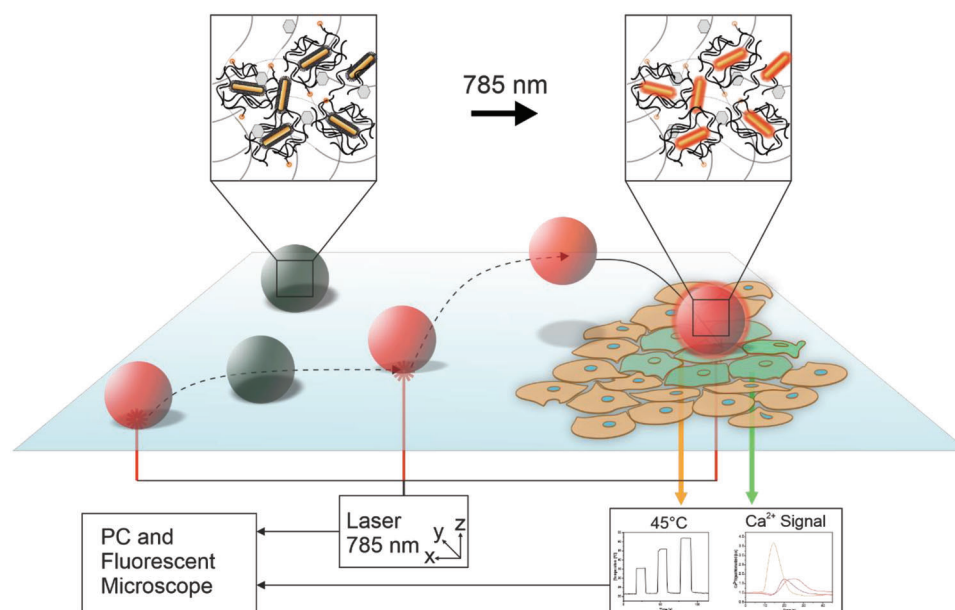


**Figure 1.** Schematic representation of TACSI microrobots. Single microrobots are actuated via laser light in 3D workspace, which allows spatiotemporal control over locomotion and heat generation. An integrated thermoresponsive nanosensor provides real-time temperature feedback, while active localized heating leads to thermal actuation of single cells. The system allows measurement of dynamic cellular changes such as intracellular calcium content in parallel.

microscopy techniques, this approach recently led to the discovery of cold and warm responsive cortical neurons in mice.<sup>[12]</sup> While heating elements are suitable for large scale studies, they typically suffer from hysteresis in heating–cooling cycles, and spatial variations in temperature, which limits spatiotemporal resolution. To address these issues, alternative approaches relying on infrared lasers, microfluidic devices, and light-sensitive small-scale heaters have been developed.<sup>[13–17]</sup> Among these, plasmonic nano- and microheaters are particularly attractive, since they provide precise temperature control, rapid heating–cooling performance without hysteresis, ability to provide a wide range of temperatures, and high spatial resolution.<sup>[18–21]</sup> Specifically, plasmonic gold nanomaterials have been used to investigate the dynamic influence of temperature on integrin signaling, heat shock protein formation, apoptosis, and activation of voltage-gated ion channels at the single cell level.<sup>[17,22–25]</sup> Despite their remarkable performance, plasmonic small-scale heaters alone are incapable of providing 3D cell culture conditions relevant to native tissue, which is now widely accepted as a crucial requirement for cell culture. Integrating plasmonic nanodevices in cell life supporting biomaterials was recently proposed as an alternative, which demonstrated that gold nanorods retain their photothermal actuation capabilities when embedded in 3D hydrogel scaffolds.<sup>[26]</sup> However, this approach is not easily adaptable to different cell types in varying cell culture conditions.

Soft microrobots can overcome challenges related to adaptability and biointegration, by combining mobile thermometry with 3D cell culture conditions in a versatile manner. For example, optically controlled nanoactuators have been used to guide single cell migration, calcium signaling, and differentiation for a variety of different cell types *in vitro*.<sup>[20,27,28]</sup> Leveraging microrobot motility allows targeting single cells among a pop-

ulation of cells in culture without the need for any preparatory steps. Microrobots can easily be introduced into cell culture and externally-guided to specific locations to perform specific tasks *in situ*. For example, catalytic micromotors were used to apply force directly on single cells in culture, to investigate intracellular calcium signaling, T-cell activation, and prey uptake in macrophages.<sup>[29,30]</sup> Moreover, recent advances in actuation and control strategies have led to the development of microrobots capable of moving in complex, fibrillar 3D environments.<sup>[31]</sup> The fine spatiotemporal resolution of light-driven soft microrobots combined with user-controlled motility, allows targeting specific cells belonging to a population, over large distances. Sensing capabilities can be integrated on-board, to provide live feedback during actuation, as demonstrated with biomolecule and temperature sensing.<sup>[32,33]</sup> Overall, light-driven soft microrobots are capable of precise actuation and sensing, while allowing seamless integration in cellular systems.

Here, we present a novel soft microrobot, designed to target and thermally stimulate single mammalian cells, while providing real-time temperature feedback (**Figure 1**). Our Thermally Activated Cell-Signal Imaging (TACSI) microrobot is composed of gold nanorods distributed in a fluorescently labeled, hydrogel network. Plasmonic gold nanorods (GNRs) function as small-scale heaters under near-infrared light, while the thermoresponsive fluorescent dye, Rhodamine B (RhB), acts as the thermometer to provide live temperature feedback. Alginate is selected as the base material to build the TACSI microrobot, because it allows robust integration of both GNRs and fluorescent probes without affecting their performance, while maintaining cell biocompatibility.<sup>[28,34,35]</sup> We use microfluidic encapsulation to fabricate the TACSI microrobots, which enables the rapid production of thousands of microrobots with tunable properties.

The resulting TACSI microrobots can generate local temperature changes of 2 °C up to 40.9 °C, without exhibiting any significant hysteresis during heating and cooling cycles. Fine tuning of microrobot performance is achieved by varying the laser power, GNR loading in and device size. Thermophoretic convection enables locomotion in low Reynolds regimes, with speeds up to 20  $\mu\text{m s}^{-1}$  in a 3D workspace. In order to demonstrate the capabilities of our platform, we stimulate human embryonic kidney (HEK) 293 cells using TACSI microrobots and investigate intracellular calcium signaling under NIR light activation. The microrobots can precisely target single cells, and preliminary data shows a dose-dependent change in intracellular calcium content. Our results indicate the activation of thermally sensitive ion channels, offering a new way to study thermal biology in a 3D addressable and adaptable manner. Overall, TACSI microrobots are highly adaptable tools, that combine photothermal actuation, temperature sensing, locomotion, and cell stimulation.

## 2. Results and Discussion

### 2.1. Design and Microfluidic Fabrication of TACSI Microrobots

We selected alginate as the base material for constructing TACSI microrobots, due to its excellent biocompatibility, thermal stability, ease of chemical modification, and adaptability to micro-fabrication methods.<sup>[36,37]</sup> Encapsulating plasmonic nanoparticles within alginate microgels can be achieved using droplet technology, and the resulting hybrid microgels retain the optical performance of encapsulated GNRs.<sup>[28,35]</sup> Here, we specifically chose plasmonic GNRs responsive to NIR light at 785 nm, to achieve optimal microrobot performance while preventing any signal crosstalk between actuation and temperature sensing. We selected RhB as the temperature sensor due to its well-known microthermometry capabilities and ease of covalent coupling to alginate chains via carbodiimide chemistry.<sup>[28,37,38]</sup> We projected that this design would allow robust integration of photothermal heating units (GNRs) and the temperature sensor within a biocompatible base material, in a homogeneous manner. A spherical geometry for the microrobots was selected to resemble cells and to benefit from large surface to volume ratio, which would contribute to rapid heat dissipation at microrobot surface.

We fabricated TACSI microrobots using microfluidic encapsulation, a low-cost and high-throughput method that is suitable for fabricating micromachines (Figure 2a).<sup>[28,39,40]</sup> For this purpose, a pre-polymer mixture containing GNRs, RhB functionalized alginate (RhB-alginate), and calcium nanoparticles was prepared, which was subsequently flown through a two-channel microfluidic device. Droplet formation was achieved at T-junction site using a flow rate of 2  $\mu\text{l min}^{-1}$ . The low amount of acetic acid (0.04%) in oil phase was sufficient to dissolve calcium carbonate nanoparticles, which allowed ionic crosslinking of alginate chains (Figure 2b).

Prior to microfluidic encapsulation, GNRs were synthesized using seed-mediated solution growth, in the presence of silver nitrate and hexadecyltrimethylammonium bromide (CTAB) as stabilizing surfactant, as previously described.<sup>[28,39]</sup> Transmission electron microscopy (TEM) confirmed the nanorod geometry, and image analysis revealed an average size of  $93.1 \pm 4.1$  by  $28 \pm 2.7$  nm which correlated well with dynamic light scattering

(DLS) measurements (Figure 2c; Figure S1, Supporting Information; Table 1). The resulting CTAB-capped GNRs were highly stable at room temperature, without showing any obvious signs of irreversible agglomerations over the course of several weeks in the presence of excess CTAB. However, we conjectured that excess CTAB removal and surface modification on GNRs to keep nanorod stability unchanged, was necessary due to the previously reported cytotoxic effects of CTAB.<sup>[41]</sup> Two strategies were considered to remove excess CTAB from GNR solutions, which relied on either encapsulating CTAB-capped GNRs in alginate or exchanging surface ligands with polyethylene glycol (PEG). For this purpose, GNRs were physically mixed with alginate using tip sonication, and washed several times to remove excess CTAB. This approach revealed homogeneously encapsulated plasmonic nanorods in alginate nanoshells (Figure 2d). Interestingly, alginate nanoshell thickness was the same for both uncrosslinked and calcium crosslinked, alginate encapsulated GNRs. This is likely due to the strong electrostatic interaction between positively charged CTAB-capped GNRs and negatively charged alginate chains, which enables complete GNR encapsulation in both cases.<sup>[36,42]</sup> Encapsulating CTAB-capped nanorods in alginate nanoshells only led to a 5 nm shift in the near-infrared absorption peak wavelength, which did not significantly affect the optical properties of nanorods (Figure 2e). Overall, the similarity in absorbance bands indicated, that the alginate coating offers similar agglomeration protection as CTAB. On the other hand, commercially available PEG-capped GNRs exhibited similar optical properties and average sizes (Figure 2e, Table 1). Considering the importance of thermal stability in our microrobots, we next investigated the influence of temperature on GNR size using DLS. All GNR coatings were thermally stable up to at least 70 °C, without any significant change in size (Figure S2, Supporting Information).

Despite exhibiting similar thermal and optical properties, the different GNR surface modifications led to drastically different outcomes during microrobot fabrication. In particular, GNR surface charge and the pre-polymer mixing technique were crucial for rapid fabrication of homogeneous TACSI microrobots. Zeta-potential measurements on the three types of GNRs indicated a significant shift from positively charged CTAB-capped nanorods ( $45.1 \pm 1.1$  mV), to negatively charged PEG-capped ( $-11.7 \pm 1.9$  mV) and alginate coated ( $-48.5 \pm 1.1$  mV) nanorods as shown in Table 1, which correspond well with previously reported values.<sup>[42-44]</sup> Electrostatic interactions between GNRs and alginate chains directly affected GNR encapsulation efficiency (Figure 2f,g). PEG-capped GNRs were minimally incorporated in alginate microgels compared to alginate-stabilized nanorods, even when subjected to the same pre-polymer preparation steps and despite the higher loading concentration of. A clear discrepancy in GNR integration within the microrobots was visible in optical images of microrobots fabricated with PEG-capped GNRs, even at 24  $\text{mg ml}^{-1}$  (Figure S3, Supporting Information). The resulting microrobots only minimally responded to NIR light and did not show any motion capabilities. On the other hand, TACSI microrobots fabricated with alginate stabilized GNRs at lower nanorod concentration (5  $\text{mg ml}^{-1}$ ) exhibited much higher optical contrast indicating higher GNR encapsulation efficiency (Figure 2h). Moreover, we found that tip sonication was crucial for preparing pre-polymer mixtures to ensure high GNR

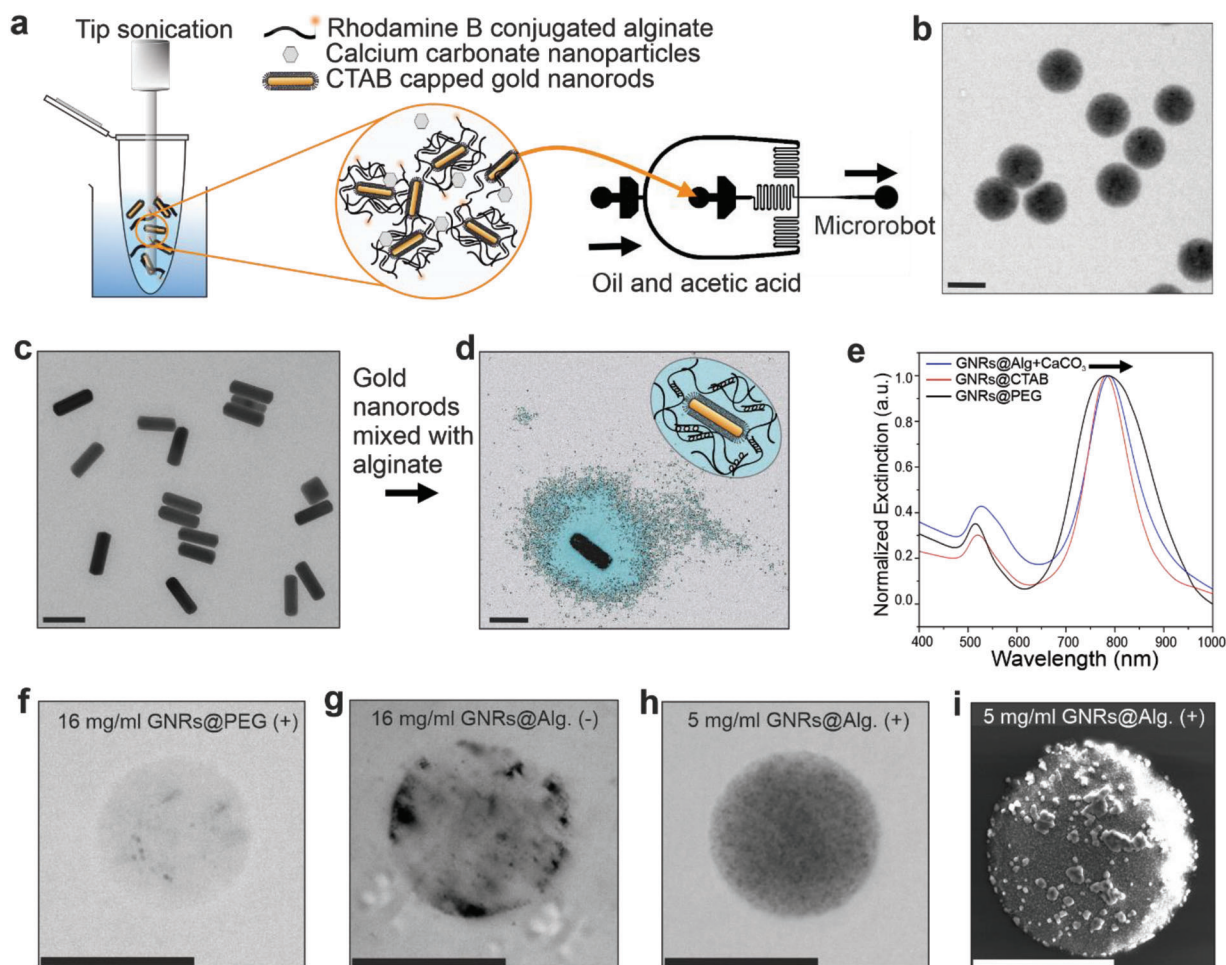


**Figure 2.** TACSI microrobot fabrication and characterization. a) Microrobots are produced via microfluidic encapsulation. A mixture of CTAB-capped GNRs (GNRs@CTAB) and uncrosslinked alginate is subjected to tip sonication prior to microfluidics. Microrobots are fabricated by flowing the pre-polymer mixture against the oil and acetic acid phase using a two-channel device. b) An exemplary brightfield image of a group of TACSI microrobots is shown. Scale bar: 30  $\mu\text{m}$ . c) A selected TEM image of GNRs@CTAB is provided. Scale bar: 100 nm. d) Colored TEM image of a single CTAB-capped GNR, encapsulated in alginate with calcium (GNR@Alg.+CaCO<sub>3</sub>), showing a layer of polymer around the nanorod is provided, with a schematic representation of the hydrogel coating. Scale bar: 100 nm. e) UV-vis spectra of different GNRs with their normalized extinction maxima at 785 nm, black arrow indicates a shift of 5 nm for the GNRs@Alg.+CaCO<sub>3</sub>. Exemplary brightfield images of single microrobots fabricated at f) 16 mg ml<sup>-1</sup> PEG-capped GNRs (GNRs@PEG) with tip sonication (+), g) 16 mg ml<sup>-1</sup> of GNRs@CTAB without tip sonication (-), h) 5 mg ml<sup>-1</sup> of GNRs@Alg.+CaCO<sub>3</sub> with tip sonication (+). Scale bars: 15  $\mu\text{m}$ . i) SEM image of a microrobot, fabricated with 5 mg ml<sup>-1</sup> of GNRs@Alg.+CaCO<sub>3</sub> (+). The micron sized clusters on the microrobot belong to the sputtered gold layer prior to imaging. Scale bar: 15  $\mu\text{m}$ .

encapsulation, and ensuring homogeneous nanorod distribution in the resulting TACSI microrobots (Figure 2i). Overall, encapsulating CTAB-capped GNRs within alginate, retained the optical properties and aqueous stability of GNRs. Vigorously mixing the pre-polymer mixture prevented agglomerations and blockage in the device channels during the microfluidic process, enabling the fabrication of  $\approx 100000$  TACSI microrobots in less than an hour. With this approach, microrobots with homogeneously distributed GNR nanoheating elements were rapidly produced (Figure S4 and Movie S1, Supporting Information).

## 2.2. NIR Light Actuation and Photothermal Performance

Next, we investigated the photothermal performance of TACSI microrobots using a customized setup consisting of

**Table 1.** Hydrodynamic radius and zeta-potential measurements of different gold nanorods.

Type of Nanorod	Dimensions [nm]	Zeta-Potential [mV]
GNRs@CTAB	23.6 $\pm$ 3.4 $\times$ 95.6 $\pm$ 15.1	45.1 $\pm$ 1.9
GNRs@PEG	24.6 $\pm$ 2.2 $\times$ 87.0 $\pm$ 11.4	-11.7 $\pm$ 0.1
GNRs@Alg.	384.3 $\pm$ 154.4	-48.5 $\pm$ 1.1
GNRs@Alg.+CaCO <sub>3</sub>	362.1 $\pm$ 122.5	-45.7 $\pm$ 1.6

a 785 nm NIR laser source coupled to a fluorescence microscope (Figure 3a). Acknowledging the importance of signal uniformity, on accuracy of temperature measurements, we first evaluated the spatial distribution of RhB intensity within single microrobots.

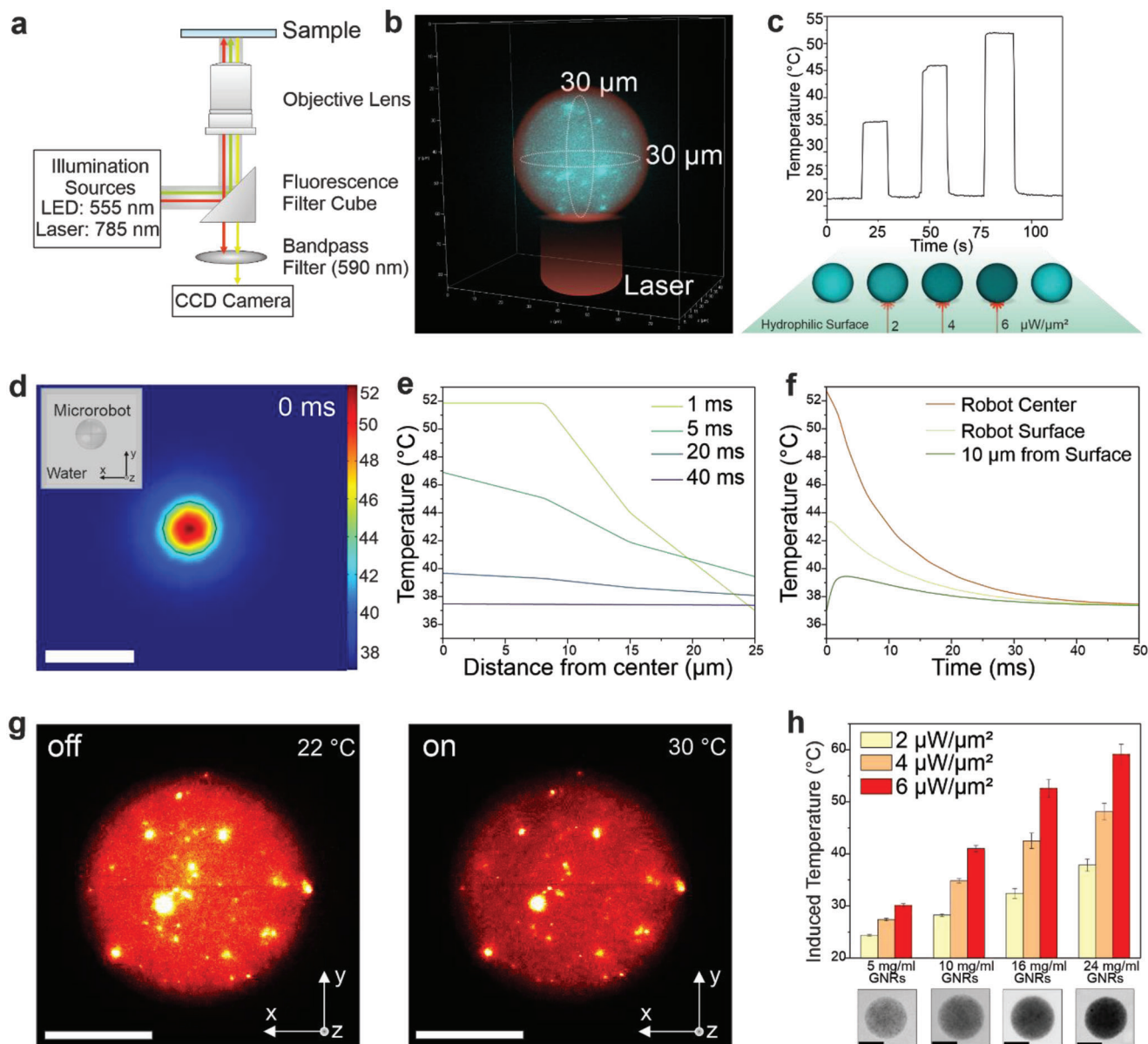


**Figure 3.** Photothermal performance of TACSI microrobots. a) Schematic overview of the experimental laser actuation and fluorescence imaging set up. Laser light is blocked during imaging via a 590 nm band pass filter inserted in front of the CCD camera. b) A representative, reconstructed 3D image of a single microrobot shows uniform spherical shape and even distribution of RhB signal. c) Graph presents representative heating cycles belonging to a single TACSI microrobot, loaded at  $16 \text{ mg ml}^{-1}$  GNR concentration, at different laser power densities. Laser power to temperature conversion was performed using the RhB calibration curve. d) Simulated heat map and e, f), corresponding temperature profiles. Scale bar:  $50 \mu\text{m}$ . g) 3D fluorescence intensity-volume stack of a single microrobot when laser is off ( $22 \text{ }^\circ\text{C}$ ) and when laser is on ( $30 \text{ }^\circ\text{C}$ ), shows even photothermal heating throughout the volume of the microrobot. Scale bar:  $15 \mu\text{m}$ . h) Thermal output analysis of different microrobot species ( $n = 20$ ), fabricated at  $5 \text{ mg ml}^{-1}$  to  $24 \text{ mg ml}^{-1}$  GNR loading. Scale bar:  $15 \mu\text{m}$ .

Indeed, scanning a single TACSI microrobot through the  $x$ ,  $y$ , and  $z$  axes confirmed uniform RhB intensity throughout the microrobot body (Figure 3b). As expected, actuating the microrobot with the laser beam led to a significant decrease in fluorescence intensity, which quickly recovered to initial baseline when the laser was turned off. Using alginate microgels as negative control, we confirmed the change in fluorescence intensity was triggered by local heat generation, via the plasmonic effect of GNRs, and not due to light absorption by alginate chains. RhB intensity in

alginate microgels without GNRs stayed constant in the presence of NIR light. To be able to rely on RhB intensity to monitor microrobot temperature, we next calibrated TACSI microrobots using a microscope stage heater to heat microrobots within a range of  $20\text{--}55 \text{ }^\circ\text{C}$ , while simultaneously measuring RhB intensity. Fluorescence signal over 100 microrobots was recorded at increments of  $5 \text{ }^\circ\text{C}$ , using 16-bit images taken with 40x magnification to ensure high spatial accuracy (Figure S5, Supporting Information). During image acquisition, LED intensity was minimized to avoid

photobleaching. We selected a wait time of 15 min between each measurement, to ensure thermal equilibrium at the temperature set by the stage heater, and to minimize any measurement errors when establishing the calibration curve. A calibration curve was established using normalized RhB intensity values over the selected temperature range, resulting in a linear fit that correlated well with previous reports (Figure S5, Supporting Information).<sup>[26,45]</sup> Using this calibration curve, we correlated the induced temperature changes on microrobots with NIR laser power. Varying laser power density from 0 up to  $6 \mu\text{W } \mu\text{m}^{-2}$  showed stepwise increase in temperature, where both heating and cooling phases took place without any significant hysteresis (Figure 3c). This approach remarkably allowed us to observe thermal changes in a repeatable manner without any irreversible loss in fluorescence intensity, even after multiple cycles of actuation.

While the thermosensitive fluorescent probe allows us to monitor microrobot temperature during actuation, it does not provide information on heat dissipation dynamics from the microrobot surface. In the ideal case, photothermally generated heat should be closely confined to the microrobot body or surroundings, to achieve single cell targeting precision. To evaluate this point, we studied heat transfer in our system using 2D finite element modeling with COMSOL Multiphysics software. A  $30 \mu\text{m}$  microrobot was placed in water, and heat transport at solid–liquid interface was investigated following photothermal actuation (Figure 3d). Computational results at microrobot cross-section showed rapid heat dissipation in 40 ms within  $10 \mu\text{m}$  distance from microrobot surface (Figure 3d–f). Our calculations are in accordance with experimental findings, which showed rapid heating and cooling on the order of 100 ms (Figure 3c). It is important to note that 50% of the generated heat is already dissipated at a distance of  $5 \mu\text{m}$  from the microrobot surface, demonstrating locally confined heating as desired.

Following calibration and computational validation, we investigated how well TACSI microrobots can be thermally regulated. To this end, we first measured the 3D volumetric fluorescent intensity of single microrobots during laser activation under homogeneous illumination, which revealed even reduction of fluorescence throughout the microgel volume (Figure 3g). Partially actuating microrobots by focusing the 785 nm laser beam on specific regions, allowed thermal patterning.

Initial measurements on the photothermal performance of TACSI microrobots showed fine spatiotemporal control over temperature via laser power, while only hinting at thermal tunability within the system. We conjectured that fine thermal control over induced temperatures was required to apply TACSI in cell stimulation studies. This is especially important for investigating for heat-sensitive dynamics of large families of ion channels (e.g., TRP), which are known to respond to a wide range of temperatures from 38 to  $52 \text{ }^\circ\text{C}$ .<sup>[46]</sup> To this end, we systematically studied the range of TACSI induced temperatures, by varying the initial GNR loading concentration in microrobots. Four types of TACSI microrobots were fabricated using microfluidic encapsulation with GNR concentrations ranging from 5 to  $24 \text{ mg ml}^{-1}$ . Prior to fabrication, GNR solutions at different concentrations were prepared, by relying on dry mass measurements and theoretical calculations based on GNR absorbance at 400 nm. Different microrobot types with GNR loading of 5, 10, 16, and  $24 \text{ mg ml}^{-1}$  were prepared separately, using microfluidic encapsulation.

For each group, 20 microrobots were randomly selected and optically actuated, while 2D fluorescence images were simultaneously recorded, and induced temperature of single microrobots were measured by tracking changes in RhB intensity. During photothermal actuation, GNR content within the microrobot stayed fixed, and NIR-induced temperature changes were regulated by adjusting the laser power (Figure 3h). The results demonstrated a gradual increase in photothermally induced temperature for all conditions, with increasing laser power. Temperature changes as low as  $4.3 \text{ }^\circ\text{C}$  was achieved by reducing GNR concentration to  $5 \text{ mg ml}^{-1}$  and actuating TACSI microrobots at low laser power ( $2 \mu\text{W } \mu\text{m}^{-2}$ ). On the other hand, the induced temperature difference could be increased as high as  $40.9 \text{ }^\circ\text{C}$  using microrobots with  $24 \text{ mg ml}^{-1}$  GNR loading. Moreover, microrobot temperature closely followed the applied laser power, where incrementally raising the laser power in a step-wise manner enabled precise regulation of induced temperature at  $2 \text{ }^\circ\text{C}$  resolution from  $28.5$  to  $40.9 \text{ }^\circ\text{C}$  (Figure S6, Supporting Information). These findings demonstrate the versatility of the TACSI platform, where thermal loads can be precisely regulated by tuning GNR content in microrobots and by modulating laser power. Our platform enables actuation and sensing with precise spatiotemporal control, making TACSI microrobots excellent candidates for studying ion channel families.

### 2.3. Light-Driven Locomotion Using TACSI Microrobots

We experimentally determined and analyzed the different modes of microrobot mobility. Microrobot locomotion relied on thermophoretic convection generated by local plasmonic heating, which has been reported for a variety of small-scale robots.<sup>[47–49]</sup> Here, we achieved microrobot movement in 3D workspace by partially activating the microrobot to induce heat gradients, which drove fuel-free thermophoretic convection. This locomotion strategy relies on plasmonic nanoagents to generate temperature gradients in liquid, leading to the formation of local convectional flows. Complex motion patterns can be induced in a spatially precise manner via thermophoretic convection.<sup>[50,51]</sup> We used thermophoretic motion to move microrobots and investigated the influence of experimental parameters on locomotion modes. In particular, tuning the laser power and illumination area enabled the generation of different motion patterns depending on the surface conditions (Figure 4a). For example, TACSI microrobots exhibited rolling motion at the substrate–liquid interface when activated at an intermediate laser power of  $4 \mu\text{W } \mu\text{m}^{-2}$  reaching speeds of up to  $5 \mu\text{m s}^{-1}$  (Figure 4b; Movie S2, Supporting Information). Placing the laser beam asymmetrically on the microrobot induced stronger convectional flow on the activated side, causing the microrobot to roll away from the laser spot (Figure 4a, inset). A hydrophobic surface was necessary to prevent microrobot binding to the substrate and to accomplish locomotion in a reliable manner. We confirmed the generation of strong convectional flows around microrobots by tracking motion patterns of  $2 \mu\text{m}$  polystyrene beads distributed in the surrounding liquid (Figure 4c; Movies S3 and S4, Supporting Information).

While rolling motion was confined to 2D, microrobot motion in z-direction was achieved by simply illuminating the

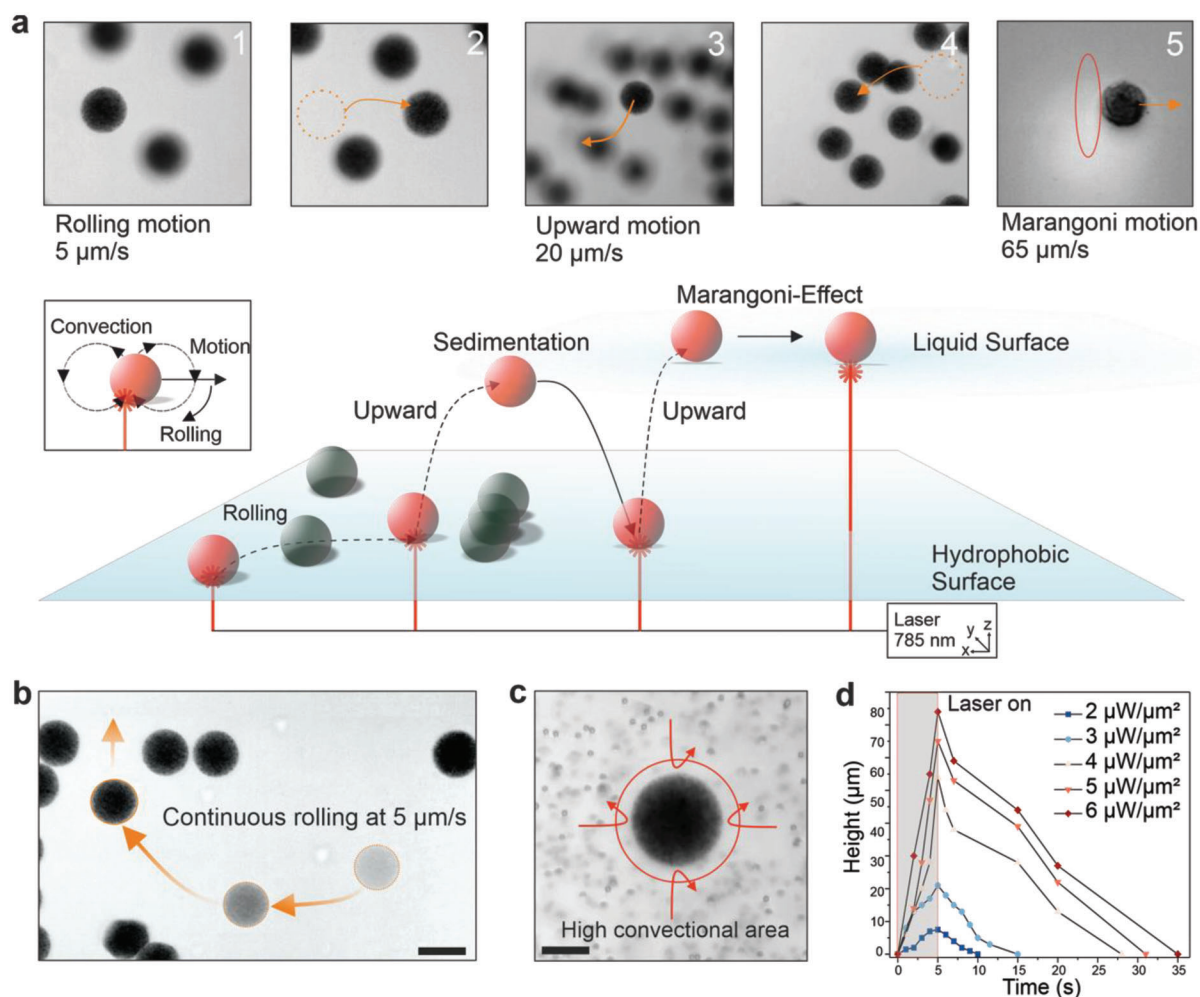


**Figure 4.** Characterization of light-driven microrobot locomotion modalities and speeds. a) Images in (1) and (2) show guided movement in  $x$  and  $y$  direction with obstacle passing at a speed of  $5 \mu\text{m s}^{-1}$ . Upward motion is depicted in (3), with microrobot moving over obstacles with a vertical speed of  $18 \mu\text{m s}^{-1}$ , and landing in (4). Image (5) shows movement at the liquid surface with recorded speeds of up to  $65 \mu\text{m s}^{-1}$ . Inset below schematically depicts the rolling motion of a microrobot away from strong convective flow. b) Steering capabilities of a single microrobot in the  $x$  and  $y$  direction. Fainter microrobots with dotted line show previous location. Scale bar:  $30 \mu\text{m}$ . c) Convective flow is visualized using  $2 \mu\text{m}$  sized polystyrene beads. Arrows indicate the high convection around the microrobot. Scale bar:  $15 \mu\text{m}$ . d) Tracked  $z$ -height of single microrobots ( $10 \text{ mg ml}^{-1}$  GNR loading) recorded with a range of laser power densities.

microrobot partially in the  $z$ -axis and focusing the laser beam at the bottom of the microrobot. The height and speed of upward motion was regulated by increasing NIR laser power and illumination time (Figure 4d). The distance covered by the microrobot in the  $z$ -axis increased at higher laser powers for the same NIR light actuation time (Figure 4d). On the other hand, microrobot altitude could be regulated by increasing illumination time at constant laser power. We recorded speeds of up to  $20 \mu\text{m s}^{-1}$  at the highest laser power with a  $75 \mu\text{m}$  height change for TACSI microrobots loaded at  $10 \text{ mg ml}^{-1}$  GNR concentration. Increasing laser power and actuation time led to stronger thermophoretic convection, which propelled the microrobots higher, consistent with previous reports.<sup>[49]</sup> Relying on upward motion, TACSI microrobots were guided around obstacles, without disturbing any stationary microrobots in the vicinity (Figure 4b). Once positioned at the liquid-air interface, microrobots exhibited Marangoni motion reaching much higher

speeds of up to  $65 \mu\text{m s}^{-1}$  (Movie S5, Supporting Information). The ability to switch between different modes of locomotion makes TACSI microrobots highly appealing for cell studies covering large distances. Moreover, photothermal actuation enabled swarm control, further enhancing the versatility of TACSI microrobots (Figure S7 and Movie S6, Supporting Information). Swarm mobility was achieved by actuating several microrobots for an extended period of time, up to 60 s at low magnification. Steady generation of convective flows pooled the microrobots towards the center of the beam spot at  $2 \mu\text{m s}^{-1}$  speed.

#### 2.4. Thermally Triggered Calcium Signaling in Mammalian Cells via TACSI

Having established microrobotic capabilities, we turned our attention to integrating TACSI platform in a biological setting.

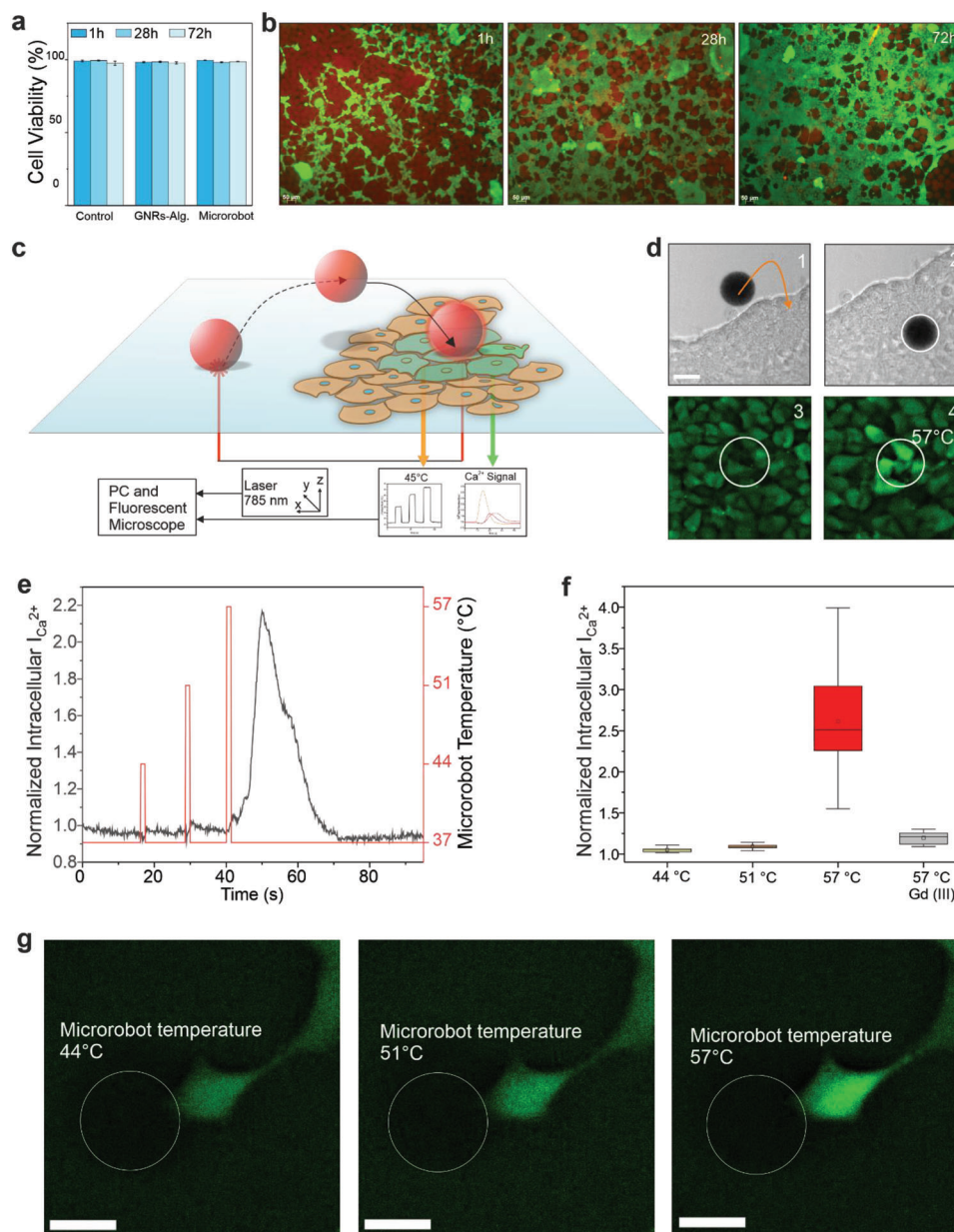


**Figure 5.** Biocompatibility and photothermal stimulation of HEK 293 cells using TACSI microrobots. a) Cell viability over 72 h for control without GNRs or microrobots, encapsulated GNRs@Alg at 10 mg ml<sup>-1</sup>, and TACSI microrobots with 10 mg ml<sup>-1</sup> GNRs@Alg loading is presented (n = 1000). b) Exemplary fluorescence images of TACSI microrobots with cells in culture. Red signal indicates microrobots while green signal shows cells. Scale bar: 50 μm. c) Schematic representation of a photothermal biostimulation event and d) corresponding experiment. Microrobot is guided onto cells in (1) and (2), and actuated via laser light following sedimentation (3). Thermal cell stimulation triggers a drastic increase in intracellular calcium signal is detected (4). Scale bar: 30 μm. e) Change in normalized intracellular calcium intensity of a single cell stimulated with a single microrobot at different laser power densities. Laser duration: 1 s. f) Cell response to different photothermal heat doses against Gd<sup>3+</sup> treated control (n = 20). Temperatures correspond to 2, 4, 6 μW μm<sup>-2</sup> in order. g) Fluorescent image of a single HEK 293 cell during three different laser power actuations. White outline indicates the position of the microrobot. Scale bar: 20 μm.

To this end, a detailed in vitro viability study was conducted with microrobots, using the well characterized human cell line HEK 293. As expected, CTAB-capped GNRs were completely cytotoxic, which was resolved by encapsulating them in alginate (Figure 5a). Both encapsulated GNRs and resulting TACSI microrobots were highly biocompatible over 72 h, maintaining cell viability at 97% (Figure 5a). Imaging the same area over 72 h

showed increased cell coverage around and under the microrobots (Figure 5b). These results corroborated our microrobot design criteria and demonstrated excellent biocompatibility.

As a proof of concept, we implemented TACSI microrobots as mobile tools to investigate cell response to varying doses of heat. For this purpose, HEK 293 cells were cultured as a single cell layer and microrobots with medium GNR loading (10 mg ml<sup>-1</sup>) were



introduced into cell culture. We chose calcium signaling as the biological readout in our system, due to the thermally sensitive nature of ion channels.<sup>[46]</sup> Acquiring images in brightfield and green fluorescence channels in parallel ensured microrobot localization in 3D workspace, while recording intracellular calcium intensity over time. To monitor intracellular calcium content, we used the live cell compatible fluorescent probe Calbryte 520 AM. Subjecting Calbryte 520 AM loaded cells to 785 nm light in the absence of microrobots, did not induce any changes in intracellular calcium intensity, indicating that the laser did not induce any undesirable heating effects on cells (Figure S8, Supporting Information). Having confirmed the suitability of our approach, we next thermally activated cells with our microrobots. As schematically shown in Figure 5c, a TACSI microrobot was guided onto a cluster of HEK 293 cells using photothermally controlled upward motion. Following sedimentation, the microrobot was actuated at  $6 \mu\text{W } \mu\text{m}^{-2}$  laser power for 1 s corresponding to a temperature difference of 20 °C. As a result, cells in contact with the microrobot responded immediately, by exhibiting a significant increase in intracellular calcium intensity (Figure 5d; Movie S7, Supporting Information). Interestingly, microrobots sitting over cells tended to move slightly during thermal biostimulation (Movie S7, Supporting Information), while TACSI microrobots directly in contact with the underlying tissue culture plastic stayed immobile. It is important to mention that mechanical impact during microrobot sedimentation was insignificant and did not induce any observable change in the underlying cells. By actuating TACSI microrobots with high laser power, we locally heated few cells from 37 to 57 °C within about 100 ms, which can be categorized as noxious heat stimulation. During this process, live temperature feedback from TACSI microrobots were successfully acquired without interfering with calcium imaging.

One of the advantages of TACSI microrobots is its tunable thermal performance, which is highly advantageous when investigating dose dependent ion channel activation. To show the full capabilities of our system, we varied the photothermally induced microrobot temperature and observed cellular response. Cells responded by exhibiting 2.15 times change in intracellular calcium intensity only when the microrobot temperature exceeded 52 °C (Figure 5e). Shortly after thermal stimulation at  $6 \mu\text{W } \mu\text{m}^{-2}$ , intracellular calcium intensity drastically increased over 15 s, and completely recovered to baseline after 30 s (Figure 5e). We hypothesized the observed cellular response could be due to activation of thermally sensitive ion channels such as TRP vanilloid 1 and 2, which are regulators of calcium signaling that can be triggered at temperatures over 52 °C.<sup>[52,53]</sup> To test this hypothesis, we stimulated 20 cells at three photothermal heat loads for 1 s and compared our findings with a negative control group, which was treated with ion channel blocker gadolinium ( $\text{Gd}^{3+}$ ). Cells stimulated with TACSI microrobots at 57 °C exhibited 2.5 times change on average while  $\text{Gd}^{3+}$  treated cells showed almost indiscernible change in calcium intensity (Figure 5f). These findings indicate the likely involvement of thermally sensitive ion channels during photothermal actuation in a dose dependent manner. We finally demonstrated high spatial precision of TACSI microrobots which can selectively target single cells (Figure 5g). Overall, TACSI microrobots allow spatiotemporally controlled biostimulation at single cell precision, offering a novel tool for thermal biology investigations.

### 3. Conclusion

We present an optically controlled and mobile soft microrobot for thermal stimulation of single mammalian cells. Constructing TACSI microrobots with alginate as base material ensures excellent biocompatibility while enabling robust integration of plasmonic nanoheaters and thermoresponsive sensor molecules. Leveraging photothermally-powered locomotion allows targeting single cells within large cell populations, and TACSI microrobots are capable of stimulating individual to clusters of cells in a spatiotemporally controlled manner. Versatile locomotion capabilities, with switchable modes of motion and varying speeds within a range of 5–65  $\mu\text{m s}^{-1}$ , are demonstrated in a 3D workspace. HEK 293 cells stimulated with TACSI microrobots exhibit calcium signaling in a heat dose dependent manner, while maintaining cell viability in vitro over several days.

Our microrobotic platform addresses device limitations in adaptability to cell culture conditions and biointegration, by bridging photothermal actuation, mobile thermometry, and cell life-supporting biomaterials. We envision the future use of TACSI microrobots in highly specialized tasks within complex 3D biological settings. This platform can be used to investigate thermal biology of mammalian cells, and future work will focus on investigations into TRP channel activation via thermal stimulation. Moreover, TACSI platform can be used to study functional differences between healthy and diseased cells, with implications in wound healing and cancer therapy. Capturing behavioral differences between healthy versus cancer cells could potentially help advance current photothermal therapies, and future work will focus on studying thermal biology of heterogeneous cell populations with TACSI microrobots. Furthermore, integrating single to clusters of cells with TACSI microrobots will likely lead to the development of new tissue engineering tools. With its tunable mobility, TACSI microrobots can be easily introduced in different culture conditions and used to probe temperature sensing dynamics of practically any mammalian cell type.

### 4. Experimental Section

**Gold Nanorod Synthesis and Characterization:** Gold nanorods were synthesized using seed mediated solution growth using a previously reported protocol.<sup>[28]</sup> Briefly, the wet chemistry process relied on a double surfactant mixture with CTAB and sodium oleate. Silver nitrate (Sigma Aldrich, 4 mM) acted as templating molecules and ascorbic acid (Sigma Aldrich, 0.064 M) was used to reduce gold chloride (Sigma Aldrich, 1 mM) in growth solution, which was reacted overnight at 31.5 °C. The nanorod shape and size was determined with TEM at 120 kV (FEI Tecnai). The optical properties were measured using UV-vis spectroscopy (Specord 50 plus, Analytik Jena) and the zeta-potential and hydrodynamic size was measured with DLS (Litesizer 500, Anton Paar). UV-vis and DLS measurements were done in ultra-pure water. The final concentrations were determined by freeze drying the stock solution to weigh gold mass, and additionally determined by the absorbance at 400 nm from the UV-vis spectra.<sup>[54]</sup> The nanorods used for cell experiments were sieved through a 0.22  $\mu\text{m}$  mesh, to ensure sterile conditions. To prepare encapsulated GNRs@Alg, excess CTAB was washed from the GNRs, and uncrosslinked alginate was added to the desired final GNR concentration. The solution was tip sonicated (Fisherbrand Model 120 Sonic Dismembrator) for 15 s at 60% amplitude. During this step, the vial was placed in a cold-water bath. GNRs@PEG were purchased from Nanopartz, main absorbance peak was at 785 nm.

**Microfluidic Device Fabrication:** Two channel microfluidic devices were fabricated via soft lithography using SU-8 3050 photoresist. Spin coating was applied to produce a 25  $\mu\text{m}$  thick coating and soft baked for 15 min. The exposure energy was set at 250  $\mu\text{J cm}^{-2}$ , then exposure baked for 5 min, and finally developed for 5 min. Thereafter, the wafer was coated in Sylgard 184 silicone elastomer, cured, inlets and outlets were punched through the PDMS elastomer, and the negative imprint was bound via plasma ashing onto a glass surface.

**Alginate Preparation and Microrobot Fabrication:** Alginate was prepared as previously reported which involved functionalization, purification, and freeze drying.<sup>[28,34]</sup> High molecular weight alginate (IG1, KIM-ICA) was functionalized with Rhodamine B Ethylenediamine (Thermo Fisher Scientific) at DS 2, subsequently dialyzed, treated with charcoal, filtered, and freeze-dried. Dried alginate was reconstituted at 2 wt.% in MES buffer prior to microfluidic microrobot fabrication. GNRs were mixed with alginate and tip sonicated, and the resulting mixture was flown through a two-channel microfluidic device connected to a syringe pump (Darwin Microfluidics). The flow rate was set to 2  $\mu\text{l min}^{-1}$  and the fabricated microrobots were collected, washed from excess oil, and stored at 4 °C.

**Microscope Platform:** An inverted optical microscope (Leica DM18) was coupled with a 785 nm laser (200 mW, Thorlabs). The laser was reflected by a dichroic mirror and guided internally through the microscope, onto the specimen. The microscope and the LEDs used for fluorescent imaging, were controlled through the Leica LAX software while the laser was controlled via an external controller (Thorlabs). For thermal calibration, a petri dish heater (Bioscience Tools) was used to apply 5 °C incremental temperature steps from room temperature up to 55 °C. The exposure time was set to 300 ms for all recorded images. Illumination was turned off during the 15 min equilibration time to avoid photobleaching. All experiments were performed at 40x magnification and between 2 and 6  $\mu\text{W } \mu\text{m}^{-2}$  laser power density. All images were normalized to the start temperature of 25 °C and the relative fluorescent intensity change was calculated up to 55 °C. The power density was measured using an external laser power meter (Thorlabs). Videos were captured using the LAX software at 24–300 fps, and movement speed was analyzed using Fiji particle tracking. Brightfield imaging was used to track microrobot movement.

**Simulations:** Numerical simulations were conducted using finite element modeling software COMSOL Multiphysics 5.5 (COMSOL Inc.). Solid–liquid heat transfer distance and time were simulated for a single microrobot. A spherical microrobot, diameter 30  $\mu\text{m}$ , was placed in a 200 by 200  $\mu\text{m}$  cube of water. Parameters for the microrobot were set to 0.57 W  $\text{mK}^{-1}$  for thermal conductivity, 1930  $\text{kg m}^{-3}$  for density, and 4000 J  $\text{kg K}^{-1}$  for heat capacity.<sup>[55]</sup> The water bath temperature was set to 37 °C, and the microrobot temperature was set to 52 °C. Cross sections were taken from the middle section of the microrobot and analyzed for temperature dissipation distance and time.

**Cell Work:** HEK 293 cells were acquired by AGCT and cultured according to manufacturer protocol. Cell culture media containing Dulbecco's Modified Eagle's Medium (DMEM/F12) with 5% Fetal Bovine Serum (FBS, Gibco) was used. Cells were fluorescently stained with LIVE/DEAD Cell Imaging Kit (488/570) (Thermo Fisher Scientific) at 2  $\mu\text{M}$  Calcein, 4  $\mu\text{M}$  Ethidium concentration. Thereafter, GNRs@CTAB, microrobots and GNRs@Alg+CaCO<sub>3</sub> were then added in a one-to-one ratio to the cells. The microrobots and the GNRs@Alg+CaCO<sub>3</sub> were washed with ethanol to ensure sterile conditions. Control, without GNRs or microrobots, and experimental conditions were observed over three days for a change in viability. For thermal stimulation, HEK cells were seeded on 96 well plates and sterile microrobots were added. Cell work was performed under a biological atmosphere, at 37 °C and 5% CO<sub>2</sub> concentration, using a stage top incubator (Bold Line, Oko Lab). For calcium measurements, cells were incubated with Calbryte 520 AM (Biomol, 4.5  $\mu\text{M}$ ) in isotonic solution for 40 min. Calbryte was subsequently removed, and cells were washed with the isotonic solution. For control, ionomycin was added to the stained cells. To block ion channels, Gadolinium (III) chloride hexahydrate (Merck, 150  $\mu\text{M}$ ) was added.

## Supporting Information

Supporting Information is available from the Wiley Online Library or from the author.

## Acknowledgements

The authors gratefully acknowledge the ONE MUNICH Project Munich Multiscale Biofabrication, funded by the Federal Ministry of Education and Research (BMBF) and the Free State of Bavaria under the Excellence Strategy of the Federal Government and the Länder. The authors furthermore thank the Bavarian High Tech Agenda for provided equipment funding.

Open access funding enabled and organized by Projekt DEAL.

## Conflict of Interest

The authors declare no conflict of interest.

## Data Availability Statement

The data that support the findings of this study are available in the supplementary material of this article.

## Keywords

gold-alginate nanocomposites, light-guided locomotion, mobile thermometry, photothermal actuation, plasmonic soft microrobots, thermal biology

Received: March 21, 2023

Revised: May 8, 2023

Published online: June 6, 2023

- [1] G. Baffou, F. Cichos, R. Quidant, *Nat. Mater.* **2020**, *19*, 946.
- [2] L. Zhao, X. Zhang, X. Wang, X. Guan, W. Zhang, J. Ma, *J Nanobiotechnology* **2021**, *19*, 335.
- [3] C. Guo, H. Yu, B. Feng, W. Gao, M. Yan, Z. Zhang, Y. Li, S. Liu, *Biomaterials* **2015**, *52*, 407.
- [4] H. Arami, S. Kananian, L. Khalifehzadeh, C. B. Patel, E. Chang, Y. Tanabe, Y. Zeng, S. J. Madsen, M. J. Mandella, A. Natarajan, E. E. Peterson, R. Sinclair, A. S. Y. Poon, S. S. Gambhir, *Nat. Nanotechnol.* **2022**, *17*, 1015.
- [5] Y. Yu, R. Tian, Y. Zhao, X. Qin, L. Hu, J.-J. Zou, Y.-W. Yang, J. Tian, *Adv. Healthcare Mater.* **2022**, *34*, 2201651.
- [6] L. Jin, X. Guo, D. Gao, Y. Liu, J. Ni, Z. Zhang, Y. Huang, G. Xu, Z. Yang, X. Zhang, X. Jiang, *Bioact Mater* **2022**, *16*, 162.
- [7] C. Li, X. He, Q. Li, M. Lv, J. Shen, L. Jin, D. He, *NPG Asia Mater.* **2023**, *15*, 3.
- [8] T. Ye, Y. Lai, Z. Wang, X. Zhang, G. Meng, L. Zhou, Y. Zhang, Z. Zhou, J. Deng, M. Wang, Y. Wang, Q. Zhang, X. Zhou, L. Yu, H. Jiang, X. Xiao, *Adv. Funct. Mater.* **2019**, *29*, 1902128.
- [9] B. Li, Y. Wang, D. Gao, S. Ren, L. Li, N. Li, H. An, T. Zhu, Y. Yang, H. Zhang, C. Xing, *Adv. Funct. Mater.* **2021**, *31*, 192010757.
- [10] M. J. Caterina, M. A. Schumacher, M. Tominaga, T. A. Rosen, J. D. Levine, D. Julius, *Nature* **1997**, *389*, 816.
- [11] G. D. Smith, M. J. Gunthorpe, R. E. Kelsell, P. D. Hayes, P. Reilly, P. Facer, J. E. Wright, J. C. Jerman, J.-P. Walhin, L. Ooi, J. Egerton, K. J. Charles, D. Smart, A. D. Randall, P. Anand, J. B. Davis, *Nature* **2002**, *418*, 186.

- [12] M. Vestergaard, M. Carta, G. Güney, J. F. A. Poulet, *Nature* **2023**, 614, 725.
- [13] E. J. G. Peterman, F. Gittes, C. F. Schmidt, *Biophys. J.* **2003**, 84, 1308.
- [14] C. Fang, F. Ji, Z. Shu, D. Gao, *Lab Chip* **2017**, 17, 951.
- [15] M. Andersson, S. Johansson, H. Bergman, L. Xiao, L. Behrendt, M. Tenje, *Lab Chip* **2021**, 21, 1694.
- [16] W.-H. Chen, T. Onoe, M. Kamimura, *Nanoscale* **2022**, 14, 2210.
- [17] H. M. L. Robert, J. Savatier, S. Vial, J. Verghese, B. Wattellier, H. Rigneault, S. Monneret, J. Polleux, G. Baffou, *Small* **2018**, 14, 1801910.
- [18] H. Nakatsuji, T. Numata, N. Morone, S. Kaneko, Y. Mori, H. Imahori, T. Murakami, *Angew. Chem., Int. Ed.* **2015**, 54, 11725.
- [19] A. Schirato, L. Moretti, Z. Yang, A. Mazzanti, G. Cerullo, M.-P. Pileni, M. Maiuri, G. D. Valle, *J. Phys. Chem. C* **2022**, 126, 6308.
- [20] Z. Liu, Y. Liu, Y. Chang, H. R. Seyf, A. Henry, A. L. Mattheyses, K. Yehl, Y. Zhang, Z. Huang, K. Salaita, *Nat. Methods* **2015**, 13, 143.
- [21] I. Pastoriza-Santos, C. Kinnear, J. Pérez-Juste, P. Mulvaney, L. M. Liz-Marzan, *Nat. Rev. Mater.* **2018**, 3, 375.
- [22] V. Maggi, F. Bianchini, E. Portioli, S. Peppicelli, M. Lulli, D. Bani, R. D. Sole, F. Zanardi, A. Sartori, R. Fiammengo, *Chem. - Eur. J.* **2018**, 24, 12093.
- [23] M. Zhu, G. Baffou, N. Meyerbröcker, J. Polleux, *ACS Nano* **2012**, 6, 7227.
- [24] K. E. Rogers, O. Nag, K. Susumu, E. Oh, J. B. Delehanty, *Bioconjugate Chem.* **2023**, 34, 405.
- [25] T. D. Cong, Z. Wang, M. Hu, Q. Han, B. Xing, *ACS Nano* **2020**, 14, 5836.
- [26] W. Yu, O. Deschaume, L. Dedroog, C. J. Garcia Abrego, P. Zhang, J. Wellens, Y. de Coene, S. Jooen, K. Clays, W. Thielemans, C. Glorieux, C. Bartic, *Adv. Funct. Mater.* **2022**, 32, 2108234.
- [27] A. N. Ramey-Ward, H. Su, K. Salaita, *Appl. Mater. Interfaces* **2020**, 12, 35903.
- [28] B. Özkale, J. Lou, E. Özgelci, A. Elosegui-Artola, C. M. Tringides, A. S. Mao, M. S. Sakar, D. J. Mooney, *Lab Chip* **2022**, 22, 1962.
- [29] S. Schuerle, I. A. Vizcarra, J. Moeller, M. S. Sakar, B. Özkale, A. M. Lindo, F. Mushtaq, I. Schoen, S. Pané, V. Vogel, B. J. Nelson, *Sci Robot* **2017**, 2, eaah6094.
- [30] D. Xie, D. Fu, S. Fu, B. Chen, W. He, D. A. Wilson, F. Peng, *Adv. Healthcare Mater.* **2022**, 11, 2200042.
- [31] M. B. Akolpoglu, Y. Alapan, N. O. Dogan, S. F. Baltaci, O. Yasa, G. A. Tural, M. Sitti, *Sci. Adv.* **2022**, 8, eabo6163.
- [32] Y. Sato, Y. Hiratsuka, I. Kawamata, S. Murata, S. M. Nomura, *Sci. Rob.* **2017**, 2, eaal3735.
- [33] K. Yoshida, H. Onoe, *Adv. Intell. Syst.* **2022**, 4, 2100248.
- [34] A. Mao, B. Özkale, N. J. Shah, K. H. Vining, T. Descombes, L. Zhang, C. M. Tringides, S.-W. Wong, J.-W. Shin, D. T. Scadden, D. A. Weitz, D. J. Mooney, *Proc. Natl. Acad. Sci. USA* **2019**, 116, 15392.
- [35] R. S. Stowers, S. C. Allen, L. J. Suggs, *Proc. Natl. Acad. Sci. USA* **2015**, 112, 1953.
- [36] K. Y. Lee, D. J. Mooney, *Prog. Polym. Sci.* **2012**, 37, 106.
- [37] S. Utech, R. Prodanovic, A. S. Mao, R. Ostafe, D. J. Mooney, D. A. Weitz, *Adv. Health. Mater.* **2015**, 4, 1628.
- [38] T. Bai, N. Gu, *Small* **2016**, 12, 4590.
- [39] B. Özkale, R. Parreira, A. Bekdemir, L. Pancaldi, E. Özgelci, C. Amadio, M. Kaynak, F. Stellacci, D. J. Mooney, M. S. Sakar, *Lab Chip* **2019**, 19, 778.
- [40] Z. Wie, S. Wang, J. Hirvonen, H. A. Santos, W. Li, *Adv. Healthcare Mater.* **2022**, 11, 2200846.
- [41] A. M. Alkilany, P. K. Nagaria, C. R. Hexel, T. J. Shaw, C. J. Murphy, M. D. Wyatt, *Small* **2009**, 5, 701.
- [42] H. Zhu, E. Prince, P. Narayanan, K. Liu, Z. Nie, E. Kumacheva, *Chem. Commun.* **2020**, 56, 8131.
- [43] Y. Wang, J. E. Q. Quinsa, T. Ono, M. Maeki, M. Tokeshi, T. Isono, K. Tajima, T. Satoh, S.-I. Sato, Y. Miura, T. Yamamoto, *Nat. Commun.* **2020**, 11, 6089.
- [44] A. Kodyan, E. Silva, J. Kim, M. Aizenberg, D. J. Mooney, *ACS Nano* **2012**, 6, 4796.
- [45] Y. Wu, J. Liu, J. Ma, Y. Liu, Y. X. Wang, D. Wu, *ACS Appl. Mater. Interfaces* **2016**, 8, 14396.
- [46] H. P. Fallah, E. Ahuja, H. Lin, J. Qi, Q. He, S. Gao, H. An, J. Zhang, Y. Xie, D. Liang, *Front. Pharmacol.* **2022**, 13.
- [47] H.-R. Jiang, N. Yoshinaga, M. Sano, *Phys. Rev. Lett.* **2010**, 105.
- [48] L. Lin, X. Peng, M. Wang, L. Scarabelli, Z. Mao, L. M. Liz-Marzán, M. Becker, Y. Zheng, *ACS Nano* **2016**, 10, 9659.
- [49] N.-D. Dinh, R. Luo, M. T. A. Christine, W. N. Lin, W.-C. Shih, J. C.-H. Goh, C.-H. Chen, *Small* **2017**, 13, 1700684.
- [50] J. B. Roxworthy, A. M. Bhuiya, S. P. Vanka, K. C. Toussaint Jr., *Nat. Commun.* **2014**, 5, 3173.
- [51] Y. Wenwu, B. F. Wang, S. Tang, Q. Zhou, Y. Dong, *Phys. Fluids* **2022**, 34, 043309.
- [52] F. Zhang, A. Jara-Oseguera, T. Chang, C. Bae, S. M. Hanson, K. J. Swartz, *Proc. Natl. Acad. Sci. USA* **2018**, 115.
- [53] M. P. Neeper, Y. Liu, T. L. Hutchinson, Y. Wang, C. M. Flores, N. Qin, *JBC* **2007**, 282, 15894.
- [54] L. Scarabelli, A. Sánchez-Iglesias, J. Pérez-Juste, L. M. Liz-Marzán, *J. Phys. Chem. Lett.* **2015**, 6, 4270.
- [55] H. F. Hassan, H. S. Ramaswamy, *J. Food Eng.* **2011**, 107, 117.